nature energy

Article

https://doi.org/10.1038/s41560-023-01233-8

Eutectic salt-assisted planetary centrifugal deagglomeration for single-crystalline cathode synthesis

Received: 13 September 2022

Accepted: 23 February 2023

Published online: 30 March 2023

Check for updates

Moonsu Yoon[1,2,5], Yanhao Dong[3,1,5], Yimeng Huang[4], Baoming Wang[1], Junghwa Kim[4], Jin-Sung Park[1], Jaeseong Hwang[2], Jaehyun Park[2], Seok Ju Kang[2], Jaephil Cho[2] ✉ & Ju Li[1,4] ✉

Single-crystalline layered cathodes are often desirable for advanced lithium-ion batteries. However, constrained by the accessible temperature range to prevent lithium evaporation, lattice defects and particle agglomerations, the production of single-crystalline cathodes with high phase purity, good electrochemical performance and scalability remains challenging. Here we invent a new mechanochemical activation process that offers a general solution to the conundrum of synthesizing coarse single-crystal cathodes with Li-/Mn-rich or Ni-rich chemistry, which differs from the equipment- and energy-intense and long-duration mechanochemical routes that are difficult to scale up. Our approach is based on interfacial reactive wetting, mediated by transient eutectic salts in situ melted by moderate mechanical agitations, to form a colloidal suspension of nanosized oxides dispersed in liquified lithium salts. It efficiently deagglomerates the polycrystalline precursors, repacks the crystals and homogenizes the lithium-salt distribution, thus enabling facile particle coarsening later into the single-crystalline morphology with improved electrochemical performance.

The ever-increasing demand for energy storage in automotive and other applications requires advanced lithium-ion batteries (LIBs) with higher energy density, longer cycle life and superior safety[1,2]. As cost reduction is a key driving force, scalable synthesis is required. For LIB cathodes, state-of-the-art Ni-rich layered oxides[3–5] and the emerging Li-/Mn-rich layered oxides[6–8] both adopted polycrystalline morphologies, consisting of fine-grained primary particles (around 100 to 200 nm grain size) and assembled secondary particles (around 10 μm diameter). The microstructure is designed to increase the cycle life and volumetric energy density[9]. It is compatible with the industrialized co-precipitation technique that ensures uniform transition-metal (ternary or more) distributions, high reaction activity and low lithiation temperature with the hydroxide/carbonate lithium salts. However, these polycrystalline cathodes are prone to intergranular cracking during electrode calendering and battery cycling, which electronically isolates active materials, exposes unprotected fresh surfaces to the liquid electrolyte with more side reactions and degrades the electrochemical performance[10,11].

To improve stability and reliability, synthesizing single-crystalline cathodes (micron grain-sized free-standing particles free of grain

[1]Department of Nuclear Science and Engineering, Massachusetts Institute of Technology, Cambridge, MA, USA. [2]Department of Energy Engineering, School of Energy and Chemical Engineering, Ulsan National Institute of Science and Technology (UNIST), Ulsan, Republic of Korea. [3]State Key Laboratory of New Ceramics and Fine Processing, School of Materials Science and Engineering, Tsinghua University, Beijing, China. [4]Department of Materials Science and Engineering, Massachusetts Institute of Technology, Cambridge, MA, USA. [5]These authors contributed equally: Moonsu Yoon, Yanhao Dong. ✉e-mail: jpcho@unist.ac.kr; liju@mit.edu

https://doi.org/10.1038/s41560-023-01233-8

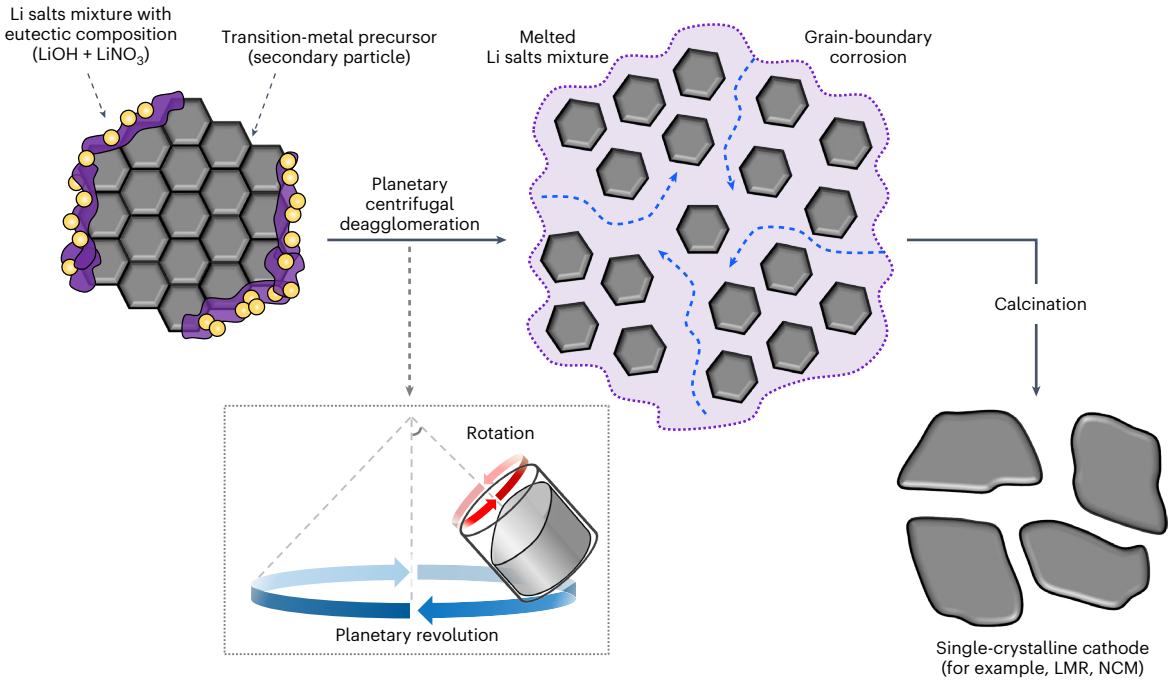

Fig. 1 | Planetary centrifugal deagglomeration for single-crystalline cathode synthesis. In the process, the transient molten Li salts (purple) corrode the grain boundaries (blue dashed arrows) of the transition-metal-oxide precursor (grey hexagons) and separate approximately ten micron-sized secondary particles into nano-sized primary ones. The molten salts, that is, a mixture of LiOH and $LiNO_3$ at/near the eutectic composition, serve as a corrosive liquid during the planetary centrifugal deagglomeration process and the Li source during the calcination process of layered cathode synthesis. Successful examples include Li-/Mn-rich layered cathode LMR and Ni-rich layered cathode NCM.

boundaries) has been proposed and attracted much attention recently[11–14]. Progress in producing high-performance Ni-rich single-crystalline cathodes includes multi-step high-temperature calcination, using excess lithium salt and a molten-salt flux method (for example, NaCl, KCl and Li_2SO_4, followed by additional washing and/or calcination; note these molten salts do not react with the cathodes or the precursors)[15–18]. Nevertheless, additional processing steps after calcination are still necessary, and the agglomeration of cathode particles is a major issue to be solved. A general cost-effective methodology applicable to both Ni-rich and Li-/Mn-rich families is urgently needed.

Mechanochemical synthesis is a branch of material chemistry and has unique capabilities of producing metastable phases under far-from-equilibrium conditions[19–22]. Examples in LIBs include mechanochemically synthesized Li-excess cation-disordered rock salt cathodes, where raw chemicals (precursor) are planetary ball-milled at high rates using stainless steel jars and grinding media to obtain out-of-equilibrium phase[23–25]. An obstacle to practical applications of mechanochemical synthesis is its capital and energy costs, which limit scalability. This is especially true for LIB cathodes, which must be mass produced with low cost and high reproducibility. In addition, the synthesized powders are often agglomerated with a wide size distribution and contaminated by impurities from the grinding media. Lastly, the underlying mechanisms remain poorly understood as the state variables (for example, temperature) are difficult to quantify, and real-time observations are often not available.

Here we report a planetary centrifugal deagglomeration technique that can scalably produce single-crystalline cathodes for both Li-/Mn-rich and Ni-rich compositions from homemade or commercially available co-precipitation precursors. When dry mixed with the precursors in a planetary centrifugal mixer (Fig. 1), LiOH-$LiNO_3$ salts with compositions near their eutectic point can in situ melt under inter-particle frictional forces and then reactively wet, corrode and separate the grain boundaries of the polycrystalline precursors. This deagglomerates the secondary particles into dispersed nanoparticles, effectively forming a colloidal suspension, and assists single-crystal growth in the follow-up calcination step. It requires no excess chemicals as LiOH-$LiNO_3$ can be fully utilized in the high-temperature lithiation process, thus serving as a transient liquid salt for efficient deagglomeration. High-performance single-crystalline cathodes with flexible compositions can be readily synthesized without extra steps of washing, annealing or sieving, thus minimizing the resource input, energy consumption and environmental burden of the cathode production.

Deagglomeration into nano-suspension

We employed a planetary centrifugal mixer (THINKY AR-100, maximum capacity: 140 g) in the present study, which is widely used for mixing, dispersing, deaerating and slurry making. Targeting Li-/Mn-rich layered cathode $Li_{1.2}Mn_{0.48}Ni_{0.16}Co_{0.16}O_2$ (LMR) as the final product, we first treated the coprecipitation precursor at 600 °C to obtain a spinel phase oxide M_3O_4 (M = Mn, Ni and Co) and then mixed with LiOH-$LiNO_3$ (40:60 molar ratio at the eutectic composition) in the planetary centrifugal mixer at 2,000 r.p.m. (Polypropylene containers were used without adding any grinding media.) As the time of mixing increased, we observed dramatic changes in the mixture morphology that can be easily identified visually (Fig. 2a–d), which is well correlated with the microstructure under a scanning electron microscope (SEM). Compared with the raw chemicals before mixing (Fig. 2a), the powders after 3 min planetary centrifugal mixing look uniform in colour and retain dry-powder morphology (Fig. 2b). SEM shows that the oxide precursors and the lithium salts remain in their original microstructure (Fig. 2e) and are non-uniformly distributed at few-μm scale (Supplementary Fig. 1). After 6 min mixing, however, the mixture self-assembled into bean-sized lumps (Fig. 2c). Meanwhile, the secondary-particle microstructure of the oxide particles is partially destroyed (Supplementary Fig. 2) and the lithium salts are uniformly distributed in the fine oxide-particle matrix at sub-micron scale. Upon further mixing up

https://doi.org/10.1038/s41560-023-01233-8

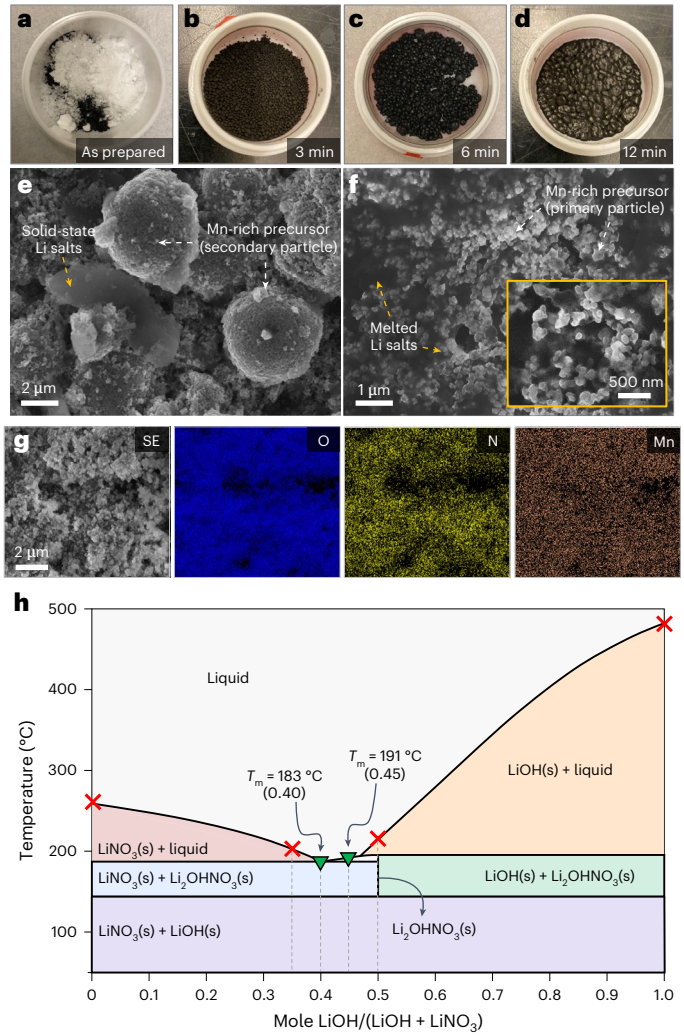

Fig. 2 | Secondary-particle deagglomeration by molten lithium salts during planetary centrifugal mixing. a–**d**, Digital images of M_3O_4 precursors and lithium salts after 0 (**a**), 3 (**b**), 6 (**c**) and 12 (**d**) min planetary centrifugal mixing. **e**,**f**, SEM images of the powder mixture after 3 min (**e**) and 12 min (**f**) mixing. **g**, Secondary electron (SE) image and EDX mapping of O, N and Mn of the powder mixture after 12 min mixing. **h**, Phase diagram of LiOH-$LiNO_3$ system (adapted from FactSage thermochemical software and databases)[49]. The six tested compositions of LiOH-$LiNO_3$ mixture are marked by the green triangle if the mixed salts melt and the M_3O_4 precursors are deagglomerated and by the red cross if not (T_m denotes melting point).

to 12 min, the powders look like solidified liquids (Fig. 2d), and under SEM, we found the primary particles of the M_3O_4 precursors are well dispersed in the matrix of LiOH-$LiNO_3$ eutectic (Fig. 2f and Supplementary Fig. 2). In other words, the secondary particles completely separated and got embedded into a liquid-like viscous matrix. Energy dispersive X-ray (EDX) mapping shows uniform elemental distributions (O, N and Mn; Fig. 2g), thus the oxide/lithium salts are uniformly distributed at a fine scale.

Along with the drastic microstructure changes, we observed interesting phase evolution in the mixture by X-ray diffraction (XRD). As shown in Supplementary Fig. 3, the oxide precursors remain in the same spinel phase before and after the planetary centrifugal mixing. However, the intensities of the peaks for lithium nitrate become much weaker after 12 min mixing. (Note the XRD results are not in situ but collected ex situ and at room temperature). Together with the microstructural features, we propose that the LiOH-$LiNO_3$ eutectic melts during the planetary centrifugal mixing process after a certain time and cannot fully crystallize after cooling down to room temperature. This is surprising given the fact that the planetary centrifugal mixing reaches an 'effective' temperature higher than the melting point of LiOH-$LiNO_3$ eutectic (T_m = 183 °C) simply from the frictional forces between the mixed particles. Meanwhile, there were no visible damages to the polypropylene containers in which the dry powders were mixed. Therefore, the 'effective' high temperature is more likely to hold locally and dynamically, while the global temperature of the container remains lower. Such in situ formed eutectic liquids, that is, molten salts, should be the key to the efficient and spontaneous deagglomeration and formation of the colloidal suspension.

We next quantified the 'effective' temperature during the planetary centrifugal mixing at 2,000 r.p.m. Varying the salt compositions across the equilibrium LiOH-$LiNO_3$ phase diagram (Fig. 2h), we confirmed by the visual morphology and SEM (Supplementary Fig. 4) that LiOH-$LiNO_3$ mixtures with mole ratios of 0:100 (T_m = 255 °C), 35:65 (T_m = 202 °C), 50:50 (T_m = 210 °C) and 100:0 (T_m = 462 °C) cannot melt or deagglomerate the oxide precursors after 12 min at 2,000 r.p.m., while the ones with 40:60 (T_m = 183 °C) and 45:55 (T_m = 191 °C) can. These control experiments narrow down the 'effective' temperature to a range of 191–202 °C, which offers insights for designing and utilizing similar processes for a variety of applications. For example, other low-melting-point salt systems can be chosen, and the 'effective' temperature can be raised by adding some zirconia balls as the inertial energy media. Lastly, as the raw chemical LiOH contains crystalline water and $LiNO_3$ is sensitive to moisture, water may also contribute to the melting and deagglomeration event, which in effect shifts the solid/liquid equilibrium at a fixed lithium-salt composition.

Mechanochemistry at nanoscale

For an atomistic understanding of the facile deagglomeration process, we conducted transmission electron microscopy (TEM) on the M_3O_4 precursors before and after the planetary centrifugal mixing. The cross-sectional image in Fig. 3a shows polycrystalline morphology of the secondary particles with densely packed/bonded primary particles before the mixing treatment. The high-angle annular dark-field scanning transmission electron microscope (HAADF-STEM) image in Fig. 3b shows that the surface and lattice of the M_3O_4 precursors have the same spinel structure, with the interlayer distance between the neighbouring lattice plane measured as 0.485 nm corresponding to the (101) lattice fringe of M_3O_4-type spinel oxide. In comparison, after 12 min mixing, the cross-sectional image in Fig. 3c shows that the primary particles are nicely separated, with the original grain boundaries corroded by and filled with the molten lithium salts (which have weak TEM contrasts yet still bond the oxide particles together in the lifted-out TEM sample; more examples shown in Supplementary Fig. 5). The HAADF-STEM image in Fig. 3d shows disordered rock-salt phase $Li_{1-x}M_xO$ (with the lattice fringe changed to 0.241 nm) at the surface of the thus-treated oxide particles (the bulk spinel phase is also confirmed). Using a density of 1.7 g cm^{-3} for the eutectic lithium salt[26] and 4.59 g cm^{-3} for the spinel oxide, we estimated the volume ratio of the eutectic to the oxide is about 3:1, which is sufficient for wetting and complete separation of the primary particles of the oxide.

We further confirmed that the surface phase transformation is general by multiple measurements at different particles. The high-resolution TEM (HR-TEM) image in Fig. 3e shows the surface disordered rock-salt phase with $Fm\bar{3}m$ symmetry after fast-Fourier transform (FFT) and the bulk spinel phase with $Fd\bar{3}m$ symmetry after FFT[27]. The atomic-resolution STEM image in Fig. 3f shows different atomic packing of the transition-metal elements that can be assigned to disordered rock-salt phase at the surface and spinel phase in the bulk. The electron energy loss spectroscopy line scan in Supplementary Fig. 6 shows varying Li content and chemical signals of Mn and O from the bulk to the surface. Therefore, we conclude that the molten lithium

https://doi.org/10.1038/s41560-023-01233-8

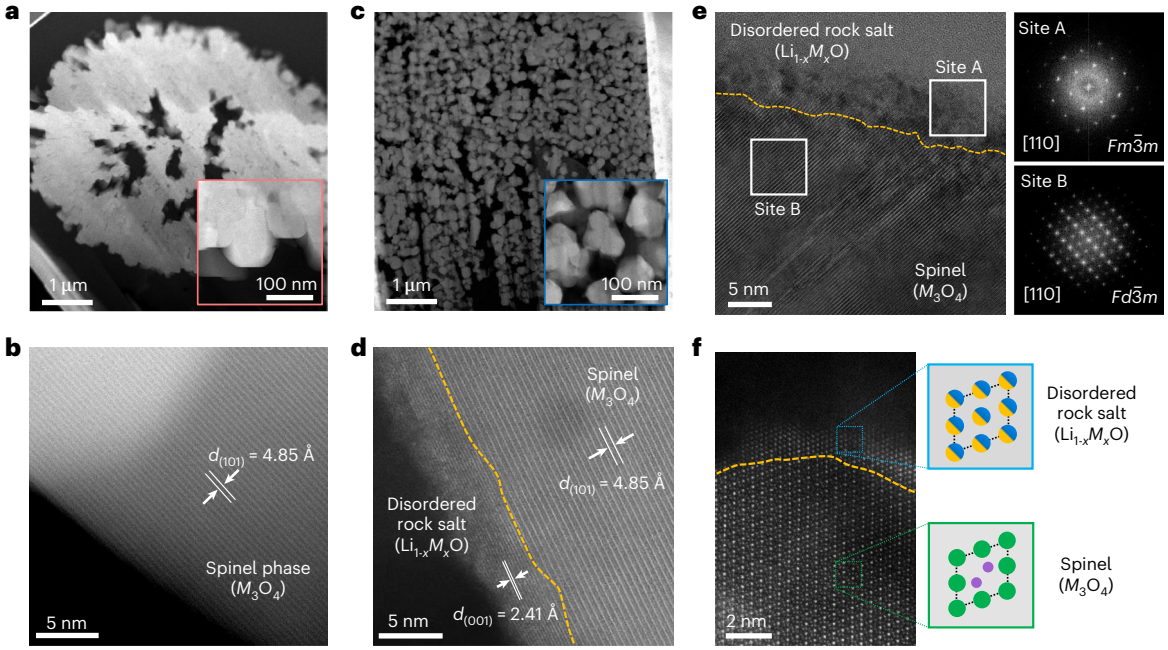

Fig. 3 | Mechanochemical reactive wetting at nanoscale. a,**b**, Cross-sectional HR-TEM (**a**) and HAADF-STEM (**b**) images of the M_3O_4 precursor with a spinel phase. **c**,**d**, Cross-sectional (**c**) and HAADF-STEM (**d**) images of the M_3O_4 precursor planetary centrifugally mixed with eutectic lithium salt, showing spinel phase in the bulk with disordered rock-salt phase at the surface. **e**, HR-TEM image and corresponding FFT patterns (selected region site A for the surface and site B for the bulk) of the M_3O_4 precursor planetary centrifugally mixed with eutectic lithium salt. **f**, Atomic-resolution STEM image of the M_3O_4 precursor planetary centrifugally mixed with eutectic lithium salt. The yellow dashed line indicates the boundary between disordered rock-salt and spinel phases (filled circles in the schematics: Li at 4a site in yellow, transition metals at 4a site in blue, transition metals at 16d site in green and transition metals at 8a site in purple).

salts not only wet the surface and separate the grain boundaries of the oxide precursor but also react with the latter beyond the atomically thin surface, into the bulk lattice up to a few nm. (The lattice deeper in the bulk is not lithiated as shown by TEM and XRD.) Such a remarkable mechanochemical reactive wetting at the nanoscale provides a unique driving force for the deagglomeration and surface phase transformation. On the kinetic side, the lithiation of the layered cathode precursors and the phase transformation to the disordered rock-salt phase have been reported to start at 200–250 °C (ref. 28). So the ~200 °C 'effective' temperature estimated above should be enough to enable the nanoscale phase transformation.

Structure of single-crystalline LMR

The planetary centrifugal mixing enables the synthesis of high-performance single-crystalline cathodes. To set a reference, we first calcinated the M_3O_4 precursors hand mixed with the lithium salts (LiOH-$LiNO_3$ at the eutectic composition, without the planetary centrifugal mixing treatment) at 940 °C for 12 h. Despite the extended calcination time, it results in polycrystalline LMR (PC-LMR) with fine primary particles (~100–200 nm; Fig. 4a). TEM-energy dispersive spectroscopy (EDS) mapping under high magnifications in Fig. 4b shows non-uniform transition metal distribution (Ni segregation and Mn and Co depletion) near the surface of PC-LMR. Supplementary Fig. 7a–c shows more examples of non-uniform Ni distributions in PC-LMR. The Ni segregation behaviours correlate with rock-salt-like phase (~2–4 nm) formed at the surface of PC-LMR (Supplementary Fig. 8a,b)[29]. In comparison, the nanoscale colloidal suspension, that is, deagglomerated M_3O_4 precursors with uniformly infiltrated lithium salts, enables the production of single-crystalline LMR (SC-LMR) cathode powders. We calcinated the planetary centrifugally mixed powders using LiOH-$LiNO_3$ eutectic at 940 °C for 2 h and 760 °C for 10 h to obtain SC-LMR with larger particle size (~1 µm) and without any secondary-particle morphology (Fig. 4c; detailed comparisons of the chemical compositions, Brunauer–Emmett–Teller surface areas and particle-size distributions measured by the particle-size analyser are available in Supplementary Tables 1 and 2). TEM-EDS mapping results (Fig. 4d and Supplementary Fig. 7d) show uniform Ni, Co and Mn distributions without surface enrichment/depletion in SC-LMR. The rock-salt-like surface phase is also much thinner in SC-LMR (~1 nm, Supplementary Fig. 8c,d), indicating a high quality of the final lithiation reaction step.

The faster particle-growth kinetics after the planetary centrifugal mixing highlights the critical role of the lithium-salt distribution and the packing of the M_3O_4 oxide precursor particles. The shorter calcination time at 940 °C helps minimize oxygen loss and Ni reduction, thus mitigating the transition-metal segregation and surface phase transformation[29–31]. The migrating surface during the Ostwald ripening process would refresh the lattice compositions and homogenize the transition-metal distributions, thus helping to eliminate the undesirable segregations and phase transformations at the surface. It also profoundly affects the phase morphology and cation ordering in the lattice. Figure 4e compares the XRD of PC-LMR and SC-LMR, where SC-LMR has wider full width at half maximum (FWHM) of the superlattice peaks at 20°–25°, indicating less Li/Mn ordering ($LiMn_6$ honeycomb ordering as is the case in Li_2MnO_3; Rietveld analysis in Supplementary Fig. 9 and Supplementary Table 3) in the lithium layer[32]. It is further supported by atomic-resolution STEM images measured along the [100] monoclinic direction, where PC-LMR shows clearer Li/Mn ordering (inferred from the clear dumbbell-like bright spots; Fig. 4f) than SC-LMR (Fig. 4g)[33]. The same trend can be observed in atomic-resolution STEM images collected over large areas (Supplementary Fig. 10). These surface and lattice structural features affect the electrochemical performance, especially the cycling stability.

https://doi.org/10.1038/s41560-023-01233-8

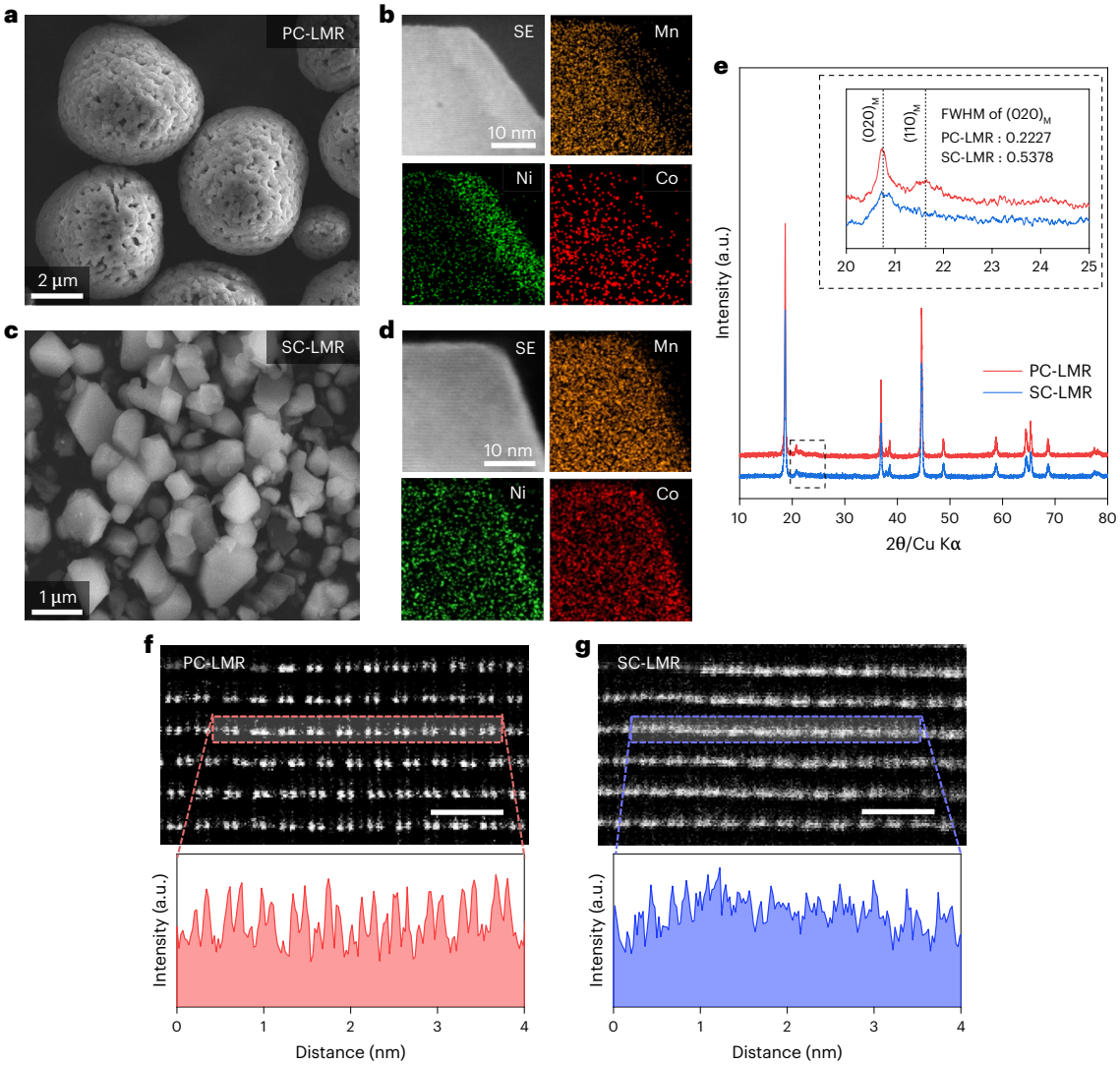

Fig. 4 | Structural characterizations of micro-sized single-crystalline LMR. **a**–**d**, SEM images and TEM-EDS mapping (Mn, Ni and Co) on cross-sectional particles of PC-LMR (**a**,**b**) and SC-LMR (**c**,**d**). **e**, Comparison of XRD patterns of PC-LMR (red) and SC-LMR (blue). Superlattice peaks and FWHM for $LiMn_6$ ordering at 20–25° are highlighted in the inset of **e**. **f**,**g**, Atomic-resolution STEM images measured along the [100] monoclinic direction of PC-LMR (**f**) and SC-LMR (**g**). Scale bars are 1 nm in **f** and **g**.

Electrochemistry of single-crystalline LMR

We next investigated the electrochemical performance of PC-LMR and SC-LMR as LIB cathodes. When first charged/discharged at 0.1 C (that is, the formation cycle; 1 C defined as 250 mA g^{-1}) between 2.0 V and 4.8 V (vs Li/Li^+), PC-LMR has a discharge capacity of 254 mAh g^{-1} and a first-cycle Coulombic efficiency of 76.2%. In comparison, SC-LMR has a slightly higher discharge capacity of 259 mAh g^{-1} and a higher first-cycle Coulombic efficiency of 82.4% (Supplementary Fig. 11). Upon cycling at 0.3 C for 100 cycles, SC-LMR has more stable charge–discharge curves than PC-LMR (Fig. 5a, b), better capacity retention (90.6% for SC-LMR vs 82.1% for PC-LMR), slower voltage decay (2.28 mV per cycle for SC-LMR vs 5.35 mV per cycle for PC-LMR) and better retention of the discharge energy density (84.9% for SC-LMR vs 69.9% for PC-LMR at the 100th cycle, Supplementary Fig. 12). Compared with literature reports on SC-LMR, our sample shows larger particle size, more uniform size distribution, compelling electrochemical performance (Supplementary Table 4) and less degradation in terms of gassing and transition-metal dissolution, as shall be discussed. To gain a better understanding of the improved cycling stability, we conducted galvanostatic intermittent titration technique (GITT; Fig. 5c) measurements with a titration current of 0.3 C after the 5th and 100th cycles, respectively. Here we focused on the voltage curves consisting of data after each relaxation step (solid curves in Fig. 5c), which are under quasi-equilibrium conditions and reflect the bulk redox chemistry. Clearly, the shape of the voltage curves was better maintained in SC-LMR compared with PC-LMR, indicating less structural/phase changes in the bulk. Indeed, as shown by TEM in Supplementary Fig. 13, extensive cavities formed in the lattice of cycled PC-LMR, accompanied by bulk phase transformations from layered to spinel/rock-salt phases[34]. These structural changes have been rationalized by enhanced oxygen ion mobility in the lattice and bulk oxygen loss[35,36]. In comparison, SC-LMR shows less structural changes in the lattice. More detailed GITT analysis (Supplementary Note 1 and Supplementary Figs. 14 and 15) further supports that the capacity decay in PC-LMR cathodes is mostly from the changes in the lattice redox chemistry and intragranular transport.

Without intergranular cracking that exposes extensive unprotected surfaces to the organic liquid electrolyte, the single-crystalline morphology should offer superior stability and less cathode–electrolyte side reactions. To prove this, we first measured the gas evolution during the first charge to 4.8 V (vs Li/Li^+) by in situ differential

https://doi.org/10.1038/s41560-023-01233-8

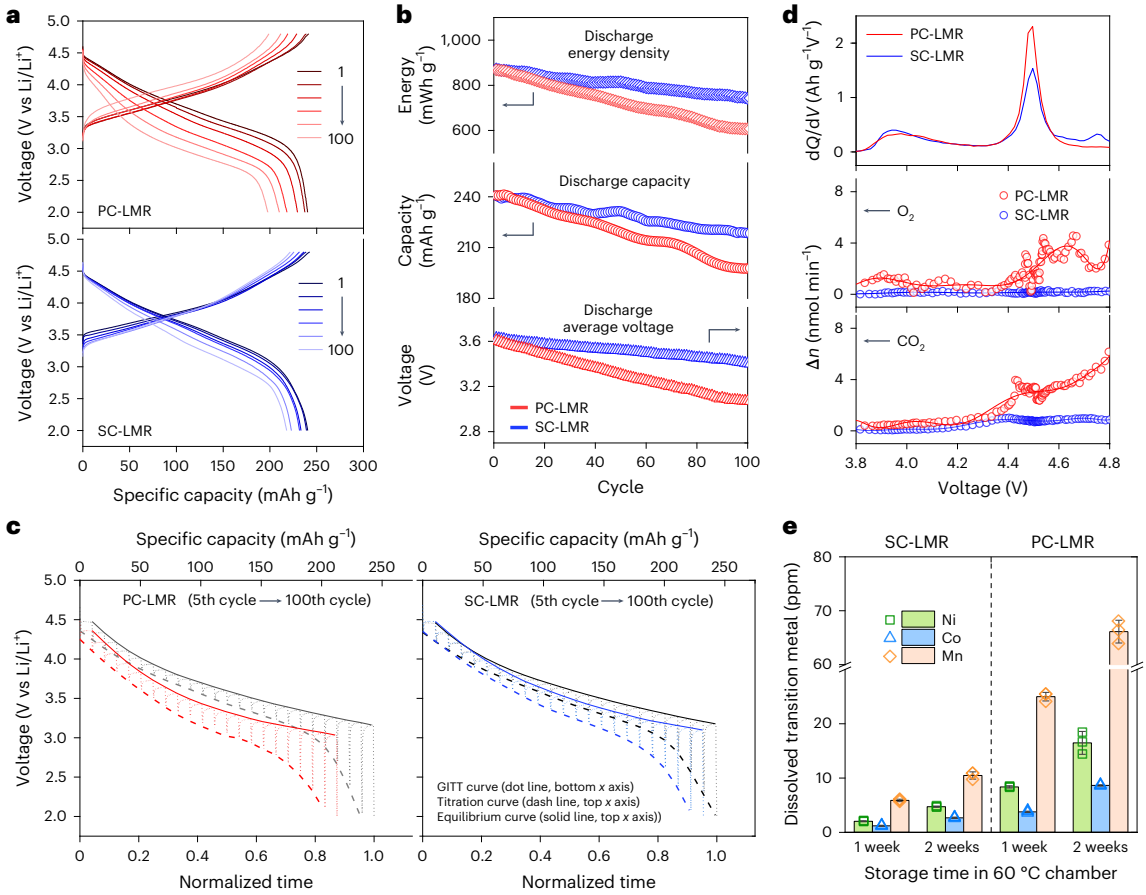

Fig. 5 | Superior electrochemical performance of SC-LMR over PC-LMR. **a**,**b**, Voltage-capacity curves (**a**) and cycling performance (**b**) of PC-LMR and SC-LMR for 100 cycles at 0.3 C (after three times of pre-cycling at 0.2 C) in the voltage range of 2.0–4.8 V vs Li/Li$^+$ at 25 °C (1 C defined as 250 mA g^{-1}). **c**, Discharge curves of GITT measurements conducted at 5th (black) and 100th (red, blue) cycles during 0.3 C cycling test. **d**, DEMS result of PC-LMR and SC-LMR during 1st cycle at 0.05 C. Differential capacity curve dQ/dV and gas evolution rate Δn are plotted. The mass spectra of mass to charge ratio $m/z = 32$ for O_2 and $m/z = 44$ for CO_2 were collected. **e**, Dissolved Ni, Co and Mn in the electrolytes measured by ICP optical emission spectrometer after one and two weeks of storage at 60 °C (the error bars in **e** are presented as ± standard deviations of dissolved transition metals in three different storage containers).

electrochemical mass spectrometry (DEMS). As shown in Fig. 5d, O_2 and CO_2 (from electrolyte decomposition when encountering freed oxygen from the cathode) start to evolve in PC-LMR charged to ~4.4 V (vs Li/Li$^+$), but their evolutions can be suppressed up to 4.8 V (vs Li/Li$^+$) in SC-LMR[37,38]. The mitigated gassing is a synergistic effect of the low specific surface area, lower-misfit-strain single-crystal lattice that does not crack and the minimized bulk oxygen loss. Consistent with the DEMS data, we found less transition-metal (Mn, Ni and Co) dissolution in the electrolytes of the charged SC-LMR cells than PC-LMR ones stored at elevated temperature (60 °C) for two weeks (Fig. 5e and Supplementary Table 5). Therefore, the coupled side reactions of gassing (oxygen loss) and transition-metal reduction and dissolution into electrolyte are indeed suppressed in SC-LMR, greatly improving the electrochemical cycling stability.

Generalization to single-crystalline Ni-rich cathode

Inspired by the single-crystalline morphology of Li-/Mn-rich cathode, we further examined the generality of our method for the synthesis of other single-crystalline cathodes. As a demonstration, we chose a Ni-rich layered cathode composition, $LiNi_{0.8}Co_{0.1}Mn_{0.1}O_2$ (NCM), of great industrial importance. Starting from the co-precipitation precursors, similar visual morphology, eutectic salt melting, microstructural change and deagglomeration outcome hold (Supplementary Fig. 16a–c). Single-crystalline NCM (SC-NCM) with ~4 μm size (Fig. 6a) can be successfully synthesized by calcinating the nanoscale colloidal suspension (hydroxide precursors plus LiOH-$LiNO_3$ eutectic, after moderate planetary centrifugation) in two-step heat treatment (920 °C for 2 h and then at 760 °C for 10 h in flowing oxygen). In contrast, when the identical lithium-salt mixture is applied without the planetary centrifugal mixing process but with hand mixing, the primary particles of the Ni-rich cathode only coarsened marginally and were sintered to form polycrystalline NCM with spherical secondary-particle morphology (treated at 800 °C for 12 h in flowing oxygen for PC-NCM in Fig. 6b and Supplementary Fig. 17; details about the chemical and physical properties are provided in Supplementary Tables 6–8). Slightly larger primary particle size can be obtained at higher temperatures, yet the secondary-particle morphology still holds (Supplementary Fig. 18a,b), which differs from the single-crystalline morphology of planetary centrifugal mixed samples treated at similar temperatures (Supplementary Fig. 18c–f). Residual porosities were also observed in some PC-NCM particles (inset of Fig. 6c), similar to some reports in the literature[28,39].

Because intergranular cracking is eliminated (Fig. 6d), SC-NCM allows harsher calendering conditions and a higher electrode density of ~3.5 g cm^{-3}, compared with ~3.1 g cm^{-3} for home-synthesized PC-NCM without causing performance degradation (Supplementary Fig. 19). Despite more severe calendering, SC-NCM is still

https://doi.org/10.1038/s41560-023-01233-8

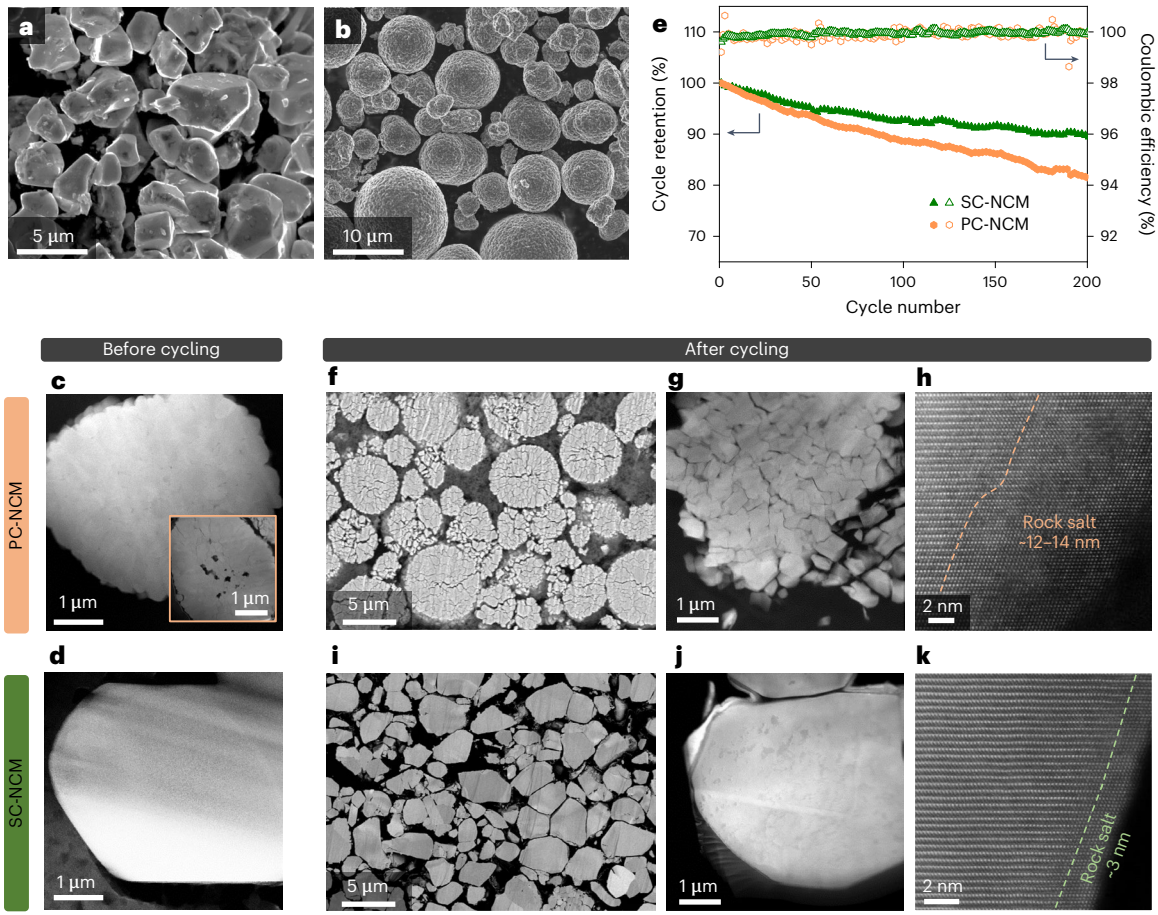

Fig. 6 | Demonstration of single-crystalline Ni-rich layered cathodes. a,**b**, SEM image of SC-NCM (**a**) and PC-NCM (b). **c**,**d**, Cross-sectional STEM images of PC-NCM (**c**) and SC-NCM (**d**). Inset of **c**: PC-NCM with residue porosities. **e**, Cycling performance of PC-NCM and SC-NCM for 200 cycles at 0.5 C/0.5 C charge/discharge rate in the voltage range of 2.8–4.3 V vs Li/Li$^+$ at 25 °C (1 C defined as 200 mA g^{-1}). **f**–**k**, Structures of PC-NCM (**f**–**h**) and SC-NCM (**i**–**k**) electrodes after cycling, characterized by cross-sectional SEM (**f**,**i**), cross-sectional STEM (**g**,**j**) and atomic-resolution STEM (**h**,**k**).

capable of delivering better capacity retention (89.7% after 200 cycles at 0.5 C/0.5 C) than PC-NCM (81.0%) (Fig. 6e and Supplementary Figs. 20–22), without any coating applied. Furthermore, compared with literature reports on Ni-rich cathode with single-crystalline morphology, our sample shows compelling electrochemical performance (Supplementary Table 9).

For PC-NCM, extensive intergranular cracking was observed in the electrode after cycling (Fig. 6f,g and Supplementary Fig. 23a,b). It leads to electronic insulation of the active cathode particles and exposes unprotected surface areas prone to various forms of side reactions (for example, thick cation-densified rock-salt-like surface phase, as shown in Fig. 6h)[40–42]. As recent works have suggested that substantial lattice mismatch with the surface-reconstruction layer could induce bulk fatigue of a Ni-rich layered cathode, the thicker surface-reconstruction layers along with the larger surface area in the PC-NCM probably induce rapid capacity decay, which is corroborated by faster impedance growth (shown by electrochemical impedance spectra, EIS, in Supplementary Fig. 24)[43–45]. In comparison, the microstructure of SC-NCM remains stable, preserving the original structural integrity even after cycling (Fig. 6i–k and Supplementary Fig. 23c,d), and side reactions are again suppressed[46,47]. The latter is well supported by the thinner rock-salt-like surface phase (Fig. 6k), less O_2 and CO_2 gas evolutions (Supplementary Fig. 25) and less transition-metal dissolution (Supplementary Fig. 26). Therefore, our mechanochemical deagglomeration method is equally applicable to the synthesis of high-performance Ni-rich single crystals.

Conclusions

Facile mechanochemical activation using a planetary centrifugal mixer for tens of minutes, instead of high-energy ball milling for hours, can induce remarkable reactive wetting of precursor oxides by a lithium eutectic salt mixture, forming a 'mechano-nanosuspension'. The well-deagglomerated nano-oxides readily react with the surrounding lithium salts at the calcination stage and coarsen into micron-sized free-standing single-crystalline powders with superior electrochemical performance by eliminating the intergranular cracking during electrode calendering and battery cycling. The suppressed oxygen evolution (up to 4.8 V charging vs Li/Li$^+$), transition-metal dissolution and voltage decay of the Li-/Mn-rich single crystals and the NCM single crystals, and the simple scalable processing, bode well for the industrialization of single-crystalline layered cathodes. Similar mechanochemical processing under relatively mild, easily accessible and well-quantified conditions should be of interest in many other applications.

Methods

Material synthesis

Hydroxide $Mn_{0.6}Ni_{0.2}Co_{0.2}(OH)_2$ was synthesized by a co-precipitation method using a continuous stirred-tank reactor. 2 M of metal solution (molar ratio Mn:Ni:Co = 3:1:1) and 4 M of NaOH solution were prepared with the stoichiometric amounts of $MnSO_4{\cdot}5H_2O$ (99.0%, JUNSEI), $NiSO_4{\cdot}6H_2O$ (99.0%, SAMCHUN), $CoSO_4{\cdot}7H_2O$ (98.0%, SAMCHUN) and $NaOH{\cdot}H_2O$ (99.0%, SAMCHUN). The reagent solutions were pumped and stirred in the continuous stirred-tank reactor at 50 °C for

10 h. The precipitates ($Mn_{0.6}Ni_{0.2}Co_{0.2}(OH)_2$) were collected, washed, dried at 120°C overnight and calcined at 600 °C for 5 h to obtain the spinel-type M_3O_4 precursors. For SC-LMR synthesis, the M_3O_4 precursors and lithium-salt mixture consisting of $LiOH{\cdot}H_2O$ (99.0%, Sigma Aldrich) and $LiNO_3$ (99.0%, Sigma Aldrich) with a molar ratio of 1:1.52 (transition metal:Li) were mixed using a planetary centrifugal mixer (AR-100, THINKY) at 2,000 r.p.m. (around 465 g force) for 12 min. This mixture was then calcinated at 940 °C for 2 h and then at 760 °C for 10 h in air to obtain SC-LMR. For PC-LMR synthesis, the M_3O_4 precursors were hand mixed $LiOH{\cdot}H_2O$ and $LiNO_3$ at the eutectic composition with a molar ratio of 1:1.52 (transition metal:Li) and annealed at 940 °C for 12 h in air.

Hydroxide $Ni_{0.8}Co_{0.1}Mn_{0.1}(OH)_2$ was synthesized by a co-precipitation method. An aqueous solution containing 3.2 M Ni^{2+}, 0.4 M Co^{2+} and 0.4 M Mn^{2+} was prepared by dissolving $NiSO_4{\cdot}6H_2O$ (99.0%, SAMCHUN), $CoSO_4{\cdot}7H_2O$ (98.0%, SAMCHUN) and $MnSO_4{\cdot}5H_2O$ (99.0%, JUNSEI) with a molar ratio of 8:1:1. The solution was continuously fed into a stirred-tank reactor (4 L capacity) with 4.0 M sodium hydroxide (NaOH) and 0.4 M ammonia (NH_4OH) solutions under feeding rates of 300, 300 and 40 ml h^{-1}, respectively. A reaction temperature of 50°C was stably maintained by an external water circulator for 20 h, after which the precipitates were collected, washed and dried at 110 °C overnight. SC-NCM was synthesized by planetary centrifugally mixing the hydroxide precursors (composition treated as $Ni_{0.8}Co_{0.1}Mn_{0.1}(OH)_2$) with $LiOH{\cdot}H_2O$ and $LiNO_3$ at the eutectic composition with a molar ratio of 1:1.025 (transition metal:Li), followed by calcination at 920 °C for 2 h and then at 760 °C for 10 h in flowing oxygen. For PC-NCM synthesis, the hydroxide precursors were hand mixed with $LiOH{\cdot}H_2O$ and $LiNO_3$ at the eutectic composition with a molar ratio of 1:1.025 (transition metal:Li), followed by calcination at 800 °C for 12 h in flowing oxygen. The venting line was tightly connected outside at the opposite side of the tube furnace to exhaust the gas naturally. Using this venting line, the gas pressure of the furnace can be maintained, and gas products (for example, toxic NO_2) are properly removed.

Electrochemical measurements

For LMR cathodes, the electrodes were prepared by mixing 80 wt% active material, 10 wt% Super-P (as the conductive agent) and 10 wt% poly(vinylidene fluoride) (as the binder) in N-methyl-2-pyrrolidone. The NCM electrodes were prepared by mixing 90 wt% active material, 5 wt% Super-P and 5 wt% poly(vinylidene fluoride) in N-methyl-2-pyrrolidone. The slurry was coated onto aluminium foil and dried at 120 °C for 10 h. All cathodes were controlled with a loading level of 10.0 ± 0.5 mg cm^{-2}. The prepared electrodes were assembled using 2032 R coin-type cell in an Ar-filled glovebox, with cathodes (diameter 12 mm), lithium-metal foils (diameter 14 mm) as the counter and reference electrode, respectively, and 1.15 M $LiPF_6$ in ethylene carbonate/ethyl methyl carbonate/diethyl carbonate with 5 wt% fluoroethylene carbonate additive (EC:EMC:DEC = 3/6/1 vol% with 5% FEC; Enchem) as the electrolyte. For LMR electrodes, the cells were evaluated with constant current-constant voltage mode between 2.0 and 4.8 V (vs Li/Li^+) at 25 °C. The first charge–discharge cycle was conducted at 0.1 C (for LMR 1.0 C is defined as 250 mA g^{-1}). After three times of pre-cycling at 0.2 C, the cells were charged/discharged at 0.3 C for 100 cycles to evaluate the cycling stability. GITT measurements were conducted after the 5th and 100th cycles of the 0.3 C cycling, between 2.0 and 4.8 V (vs Li/Li^+) with a titration step at 0.3 C of 10 min and a relaxation step of 2 h. The ohmic loss (voltage drop during the transition from the titration step to the relaxation step) and non-ohmic loss (voltage drop during the long-time relaxation step) are collected and plotted at each depth-of-discharge. For NCM cathodes, the cells were evaluated with constant current-constant voltage mode between 2.8 V and 4.3 V (vs Li/Li^+) at 25 °C. The first charge–discharge cycle (as the formation step) was conducted at 0.1 C (for NCM, 1.0 C is defined as 200 mA g^{-1}). After the first cycle, the cells were charged and discharged at 0.5 C/0.5 C for 200 cycles. After specific cycles, EIS measurements were conducted on cells charged to 4.3 V (vs Li/Li^+) from 1 mHz to 10 MHz and with AC voltage amplitude of 10 mV using VMP-300 potentiostat (Bio-logic). All electrochemical tests (except for EIS) were carried out using a CT2001A battery cycler (Landt Instrument).

Characterizations

Chemical compositions of cathode material and electrolyte were determined by an inductively coupled plasma (ICP) optical emission spectrometer (Varian 700-ES, Varian, Inc.). Specific surface areas were measured by BET analyser (Macsorb model-1208, Mountech). Phases were characterized by XRD using a parallel beam XRD instrument (Smartlab, Rigaku, with Cu Kα with a wavelength of 1.542 Å). The crystallographic analysis was conducted by using PDXL analysis software (Rigaku). Phase identification was performed using PDXL software package, including crystallography open database. Cross sections of the cathodes were cut by ion milling (IM-40000, Hitachi) and characterized under SEM (Merlin, Zeiss) equipped with EDS (XFlash 6130, Bruker) detector. Morphologies and chemical compositions of the prepared cathode powders and electrodes were also characterized by SEM and EDS. For TEM analysis, samples were prepared by a dual-beam focused ion beam (Helios 450HP, FEI) and thinned by an Ar-ion milling system (Model 1040 Nanomill, Fischione). High-resolution TEM (HR-TEM, ARM300, JEOL) was conducted under 150 keV and 300 keV to collect STEM images for atomic and structural analysis. Electron energy loss spectroscopy and EDX were conducted by HR-TEM (Aztec, Oxford). For transition-metal dissolution analysis, coin cells with as-prepared cathode and Li-metal foil (anode) were first constructed and charged to cut-off voltage (4.8 V for LMR and 4.3 V for NCM). The charged electrodes were disassembled and soaked in a clean electrolyte (3:7 by volume of EC:EMC) in an Ar-filled glovebox and transferred to an oven at 60 °C. The organic solution was stored at 60 °C, collected after one and two weeks and then under HNO_3 acid digestion following an established method[5]. The digested solution was diluted to 20 ml for the ICP measurement. The real-time gas evolution was monitored by in situ DEMS analysis under galvanostatic charge–discharge of the cell. For LMR electrodes, in situ DEMS was conducted on hole-perforated 2032-type coin cells between 2.0 V and 4.8 V (vs Li/Li^+; 2.8–4.3 V for NCM electrodes), with details described elsewhere[48].

Data availability

Data generated and analysed in the present work are available in the paper and Supplementary Information. Source data are provided with this paper.

References

1. Larcher, D. & Tarascon, J. M. Towards greener and more sustainable batteries for electrical energy storage. *Nat. Chem.* **7**, 19–29 (2015).
2. Choi, J. W. & Aurbach, D. Promise and reality of post-lithium-ion batteries with high energy densities. *Nat. Rev. Mater.* **1**, 16013 (2016).
3. Yoon, M. et al. Reactive boride infusion stabilizes Ni-rich cathodes for lithium-ion batteries. *Nat. Energy* **6**, 362–371 (2021).
4. Namkoong, B. et al. High-energy Ni-rich cathode materials for long-range and long-life electric vehicles. *Adv. Energy Mater.* **12**, 2200615 (2022).
5. Xu, G.-L. et al. Building ultraconformal protective layers on both secondary and primary particles of layered lithium transition metal oxide cathodes. *Nat. Energy* **4**, 484–494 (2019).
6. Zhang, J. et al. Addressing voltage decay in Li-rich cathodes by broadening the gap between metallic and anionic bands. *Nat. Commun.* **12**, 3071 (2021).
7. Li, H. et al. Toward high-energy Mn-based disordered-rocksalt Li-ion cathodes. *Joule* **6**, 53–91 (2022).

8. Zhang, M. et al. Pushing the limit of 3*d* transition metal-based layered oxides that use both cation and anion redox for energy storage. *Nat. Rev. Mater.* **7**, 522–540 (2022).
9. Li, W. et al. A sulfur cathode with pomegranate-like cluster structure. *Adv. Energy Mater.* **5**, 1500211 (2015).
10. Xue, W. et al. Ultra-high-voltage Ni-rich layered cathodes in practical Li metal batteries enabled by a sulfonamide-based electrolyte. *Nat. Energy* **6**, 495–505 (2021).
11. Kim, J. et al. Nickel-rich cathodes: prospect and reality of Ni-rich cathode for commercialization. *Adv. Energy Mater.* **8**, 1870023 (2018).
12. Hwang, J. et al. Lattice-oxygen-stabilized Li- and Mn-rich cathodes with sub-micrometer particles by modifying the excess-Li distribution. *Adv. Mater.* **33**, 2100352 (2021).
13. You, B. et al. Research progress of single-crystal nickel-rich cathode materials for lithium ion batteries. *Small Methods* **5**, 2100234 (2021).
14. Ryu, H.-H. et al. Capacity fading mechanisms in Ni-rich single-crystal NCM cathodes. *ACS Energy Lett.* **6**, 2726–2734 (2021).
15. Li, H. et al. Synthesis of single crystal $LiNi_{0.88}Co_{0.09}Al_{0.03}O_2$ with a two-step lithiation method. *J. Electrochem. Soc.* **166**, A1956–A1963 (2019).
16. Liu, A. et al. Synthesis of Co-free Ni-rich single crystal positive electrode materials for lithium ion batteries: part I. Two-step lithiation method for Al- or Mg-doped $LiNiO_2$. *J. Electrochem. Soc.* **168**, 040531 (2021).
17. Wang, T. et al. Synthesis and manipulation of single-crystalline lithium nickel manganese cobalt oxide cathodes: a review of growth mechanism. *Front. Chem.* **8**, 747 (2020).
18. Bi, Y. et al. Reversible planar gliding and microcracking in a single-crystalline Ni-rich cathode. *Science* **370**, 1313–1317 (2020).
19. Kubota, K., Pang, Y., Miura, A. & Ito, H. Redox reactions of small organic molecules using ball milling and piezoelectric materials. *Science* **366**, 1500–1504 (2019).
20. James, S. L. et al. Mechanochemistry: opportunities for new and cleaner synthesis. *Chem. Soc. Rev.* **41**, 413–447 (2012).
21. Friščić, T., Mottillo, C. & Titi, H. M. Mechanochemistry for synthesis. *Angew. Chem. Int. Ed.* **59**, 1018–1029 (2020).
22. Schlem, R. et al. Energy storage materials for solid-state batteries: design by mechanochemistry. *Adv. Energy Mater.* **11**, 2101022 (2021).
23. Hong, J. et al. Metal–oxygen decoordination stabilizes anion redox in Li-rich oxides. *Nat. Mater.* **18**, 256–265 (2019).
24. Clément, R. J., Lun, Z. & Ceder, G. Cation-disordered rocksalt transition metal oxides and oxyfluorides for high energy lithium-ion cathodes. *Energy Environ. Sci.* **13**, 345–373 (2020).
25. Lee, J. et al. Reversible Mn^{2+}/Mn^{4+} double redox in lithium-excess cathode materials. *Nature* **556**, 185–190 (2018).
26. Janz, G. J. Thermodynamic and transport properties for molten salts: correlation equations for critically evaluated density, surface tension, electrical conductance, and viscosity data. *J. Phys. Chem. Ref. Data* **17**, 1–309 (1988).
27. Pennycook, S. J. & Nellist, P. D. *Scanning Transmission Electron Microscopy: Imaging and Analysis* (Springer Science & Business Media, 2011).
28. Park, H. et al. In situ multiscale probing of the synthesis of a Ni-rich layered oxide cathode reveals reaction heterogeneity driven by competing kinetic pathways. *Nat. Chem.* **14**, 614–622 (2022).
29. Gu, M. et al. Conflicting roles of nickel in controlling cathode performance in lithium ion batteries. *Nano Lett.* **12**, 5186–5191 (2012).
30. Chen, H., Dawson, J. A. & Harding, J. H. Effects of cationic substitution on structural defects in layered cathode materials $LiNiO_2$. *J. Mater. Chem. A* **2**, 7988–7996 (2014).
31. Xiao, P. et al. Effects of oxygen pressurization on Li^+/Ni^{2+} cation mixing and the oxygen vacancies of $LiNi_{0.8}Co_{0.15}Al_{0.05}O_2$ cathode materials. *ACS Appl. Mater. Interfaces* **14**, 31851–31861 (2022).
32. Hwang, J. et al. Excess-Li localization triggers chemical irreversibility in Li- and Mn-rich layered oxides. *Adv. Mater.* **32**, 2001944 (2020).
33. Ku, K. et al. Suppression of voltage decay through manganese deactivation and nickel redox buffering in high-energy layered lithium-rich electrodes. *Adv. Energy Mater.* **8**, 1800606 (2018).
34. Yan, P. et al. Injection of oxygen vacancies in the bulk lattice of layered cathodes. *Nat. Nanotechnol.* **14**, 602–608 (2019).
35. Zhu, Z. et al. Gradient Li-rich oxide cathode particles immunized against oxygen release by a molten salt treatment. *Nat. Energy* **4**, 1049–1058 (2019).
36. Dong, Y., Qi, L., Alvarez, A., Li, J. & Chen, I. W. Enhanced mobility of cations and anions in the redox state: the polaronium mechanism. *Acta Mater.* **232**, 117941 (2022).
37. Freunberger, S. A. et al. Reactions in the rechargeable lithium–O_2 battery with alkyl carbonate electrolytes. *J. Am. Chem. Soc.* **133**, 8040–8047 (2011).
38. Bruce, P. G., Freunberger, S. A., Hardwick, L. J. & Tarascon, J.-M. Li–O_2 and Li–S batteries with high energy storage. *Nat. Mater.* **11**, 19–29 (2012).
39. Xiao, B. et al. Revealing the atomic origin of heterogeneous Li-ion diffusion by probing Na. *Adv. Mater.* **31**, 1805889 (2019).
40. Jung, R., Metzger, M., Maglia, F., Stinner, C. & Gasteiger, H. A. Chemical versus electrochemical electrolyte oxidation on NMC111, NMC622, NMC811, LNMO, and conductive carbon. *J. Phys. Chem. Lett.* **8**, 4820–4825 (2017).
41. Zhan, C., Wu, T., Lu, J. & Amine, K. Dissolution, migration, and deposition of transition metal ions in Li-ion batteries exemplified by Mn-based cathodes–a critical review. *Energy Environ. Sci.* **11**, 243–257 (2018).
42. Dong, Y. & Li, J. Oxide cathodes: functions, instabilities, self healing, and degradation mitigations. *Chem. Rev.* **123**, 811–833 (2023).
43. Xu, C. et al. Bulk fatigue induced by surface reconstruction in layered Ni-rich cathodes for Li-ion batteries. *Nat. Mater.* **20**, 84–92 (2021).
44. Li, W., Asl, H. Y., Xie, Q. & Manthiram, A. Collapse of $LiNi_{1-x-y}Co_xMn_yO_2$ lattice at deep charge irrespective of nickel content in lithium-ion batteries. *J. Am. Chem. Soc.* **141**, 5097–5101 (2019).
45. Liu, X. et al. Essential effect of the electrolyte on the mechanical and chemical degradation of $LiNi_{0.8}Co_{0.15}Al_{0.05}O_2$ cathodes upon long-term cycling. *J. Mater. Chem. A* **9**, 2111–2119 (2021).
46. Lin, F. et al. Profiling the nanoscale gradient in stoichiometric layered cathode particles for lithium-ion batteries. *Energy Environ. Sci.* **7**, 3077–3085 (2014).
47. Kang, Y.-S. et al. Revealing the structural degradation mechanism of the Ni-rich cathode surface: how thick is the surface? *J. Power Sources* **490**, 229542 (2021).
48. Kang, S. J., Mori, T., Narizuka, S., Wilcke, W. & Kim, H.-C. Deactivation of carbon electrode for elimination of carbon dioxide evolution from rechargeable lithium–oxygen cells. *Nat. Commun.* **5**, 3937 (2014).
49. Bale, C. W. et al. FactSage thermochemical software and databases, 2010-2016. *Calphad* **54**, 35–53 (2016).

Acknowledgements

M.Y. acknowledges support by the Basic Science Research Program through the National Research Foundation of Korea (NRF) funded by the Ministry of Education (2022R1A6A3A03069190). J.L. acknowledges support by Defense Advanced Research Projects Agency (DARPA) MINT programme under contract number HR001122C0097.

Author contributions

M.Y., Y.D., J.C. and J.L. conceived the project. M.Y. and Y.D. designed the experiments and analysed the data. M.Y. synthesized the materials and conducted electrochemical testing. Y.H. and J.-S.P. conducted SEM and ex situ XRD measurements. B.W., J.K. and J.H. conducted focused ion beam and TEM measurements. J.P. and S.J.K. conducted in situ DEMS analysis. M.Y., Y.D., J.C. and J.L. wrote the paper. All authors discussed and contributed to the writing.

Competing interests

M.Y., Y.D., J.C. and J.L declare that this work has been filed as US Provisional Patent Application (US 63/484,989). The other authors declare no competing interests.

Additional information

Supplementary information The online version contains supplementary material available at https://doi.org/10.1038/s41560-023-01233-8.

Correspondence and requests for materials should be addressed to Jaephil Cho or Ju Li.

Peer review information *Nature Energy* thanks Ke Du, Raffael Ruess and the other, anonymous, reviewer(s) for their contribution to the peer review of this work.